PNAS RESEARCH ARTICLE | CHEMISTRY

Redox dye–mediated fluorescence energy transfer of carbon nanotube–based nanosensors

Shoichi Nishitani[a], Kevin Ao[a], Amad Jalil[a], Octavio I. Arias-Soto[a], Ava Moudi[a], Feiyang Chen[a], Ankita Biyani[a], Padma N. Muppirala[a], and Markita P. Landry[a,b,c,d,e,1]

Affiliations are included on p. 8.

Edited by Catherine Murphy, University of Illinois at Urbana-Champaign, Urbana, IL; received September 27, 2024; accepted February 19, 2025

Single-walled carbon nanotubes (SWCNTs) exhibit nonphotobleaching, near-infrared (NIR) fluorescence suitable for bioimaging applications. In particular, SWCNT fluorescence quenching induced by biopolymer dispersants facilitates flexible design of molecular nanosensors, yet challenges remain in analyte selectivity and lack of rational design strategies. A sought-after alternative to haphazard molecular modulation of SWCNT-based fluorescence is to couple the movement of a quencher to the SWCNT surface, enabling fluorescence energy transfer to modulate molecular recognition with high selectivity. This study presents the rational design of SWCNT-based nanosensors with fluorescence energy transfer, leveraging the unique properties of methylene blue (MB) proximity–mediated fluorescence quenching. MB-SWCNT-based nanosensors exhibit 1- stability in redox environments and 2- analyte-specific displacement-driven fluorescence modulation. By designing hybridization-induced displacement of MB-conjugated ssDNA from the SWCNT surface, we calculate that SWCNT fluorescence modulation can occur within a 6.8 nm fluorescence resonance energy transfer distance from the SWCNT surface and develop a robust and versatile platform to synthesize oligonucleotide nanosensors with tunable $\Delta F/F_0$ of up to 150%. Building upon this strategy, we developed four distinct nanosensors capable of selectively detecting tobacco mosaic virus (TMV) viral RNA fragments, which successfully differentiated TMV-infected plants from mock controls. Finally, we demonstrate the potential expansion of our design to target a wider scope of biomolecules using the biotin-avidin system as a model. Taken together, our study presents a generalizable platform that enables rational engineering of SWCNT NIR fluorescence intensity through MB distance-dependent fluorescence energy transfer, overcoming the intrinsic selectivity challenges of current SWCNT nanosensors.

single-walled carbon nanotube | biosensor | energy transfer

Significance

Nonphotobleaching near-infrared fluorescent single-walled carbon nanotubes (SWCNTs) functionalized with ssDNA hold promise for biomedical applications. The current challenge in designing SWCNT-based nanosensors is the inability to simultaneously achieve high sensitivity and selectivity to the target analyte. This paper presents a redox dye–mediated strategy to robustly and rationally engineer SWCNT-based nanosensors. The paper finds that nm-scale physical movement of a redox dye controlled by analyte adsorption to the ssDNA enables selective recognition of a large library of analytes and performs a mechanistic investigation confirming this strategy. The paper concludes by using energy transfer to design oligonucleotide nanosensors in a manner generalizable to a wide scope of biomolecular analytes: small molecules, nucleic acids, and proteins.

Single-walled carbon nanotubes (SWCNTs) exhibit intrinsically stable, nonphotobleaching fluorescence emission within the tissue-transparent near-infrared (NIR) region, thereby rendering them particularly advantageous for biosensing and imaging applications (1, 2). Furthermore, this photoluminescence can be altered in the presence of molecular interaction at the SWCNT surface. Thus, SWCNT-based nanosensors can be designed to translate specific molecular recognition into output signals manifesting as wavelength shifts or fluorescence intensity modulations (3, 4). Specifically, certain biopolymer dispersants, including single-stranded DNA (ssDNA), can effectively quench SWCNT photoluminescence (5). This unique quenching property enables the design of nanosensors with high fluorescence turn-on/off ratios, offering significant advantages over other mechanisms such as solvatochromic wavelength shifts (6). Consequently, these nanosensors are typically designed to reverse the quenching effect in the presence of specific analytes. For instance, $(GT)_6$-wrapped SWCNTs demonstrated instantaneous fluorescence turn-on in response to dopamine, with their in vitro responses reaching 3,000% (7). Leveraging this high signal output, these nanosensors have been successfully utilized to visualize striatal dopamine release dynamics in mouse brain slices (8–10). Furthermore, systematic evolution-based screening of ssDNA facilitated the discovery of specific ssDNA sequences that confer sensitivity to other neurochemicals such as serotonin and oxytocin (11).

Although ssDNA enables effective quenching-based high turn on/off ratio with near-infinite flexibility in sequence design, challenges remain in 1) the restricted selectivity of the nanosensors, particularly in distinguishing molecules with similar redox potentials, and 2) the necessity of screening sequences that enable molecular recognition. ssDNA-based fluorescence quenching has been understood as photoinduced charge transfer processes between ionized nucleotide bases and SWCNTs, which is essentially an oxidation of SWCNTs (12). Therefore, various reducing molecules (13), including

Author contributions: S.N. designed research; S.N., K.A., A.J., O.I.A.-S., A.M., F.C., A.B., and P.N.M. performed research; S.N. contributed new reagents/analytic tools; S.N. analyzed data; K.A. provided editorial guidance; M.P.L. provided technical guidance, research prioritization, and editorial guidance; and S.N. and M.P.L. wrote the paper.

The authors declare no competing interest.

This article is a PNAS Direct Submission.

[1]To whom correspondence may be addressed. Email: landry@berkeley.edu.

This article contains supporting information online at https://www.pnas.org/lookup/suppl/doi:10.1073/pnas.2419666122/-/DCSupplemental.

Published March 20, 2025.

dopamine and other catecholamines, can intrinsically reverse the quenching, thus posing significant challenges in discriminating between molecules with similar redox potentials, exemplified by catecholamines (7). Furthermore, the unpredictable relationship between molecular recognition and signal transduction mandates sequence screening, a process which is not always guaranteed to yield operable sequences. Moreover, colloidal stability is contingent upon the ssDNA sequence, which cannot be assessed without preparing the ssDNA-SWNCT constructs. This introduces additional restrictions that compromise the versatility and robustness of SWCNT-based nanosensor design.

Alternatively, certain organic charge-transfer molecules, commonly referred to as redox dyes, can also quench SWCNT photoluminescence. For example, O'connell et al. demonstrated that organic dyes can adhere to the SWCNT surface and trigger SWCNT fluorescence quenching and that this phenomenon is partially reversible upon displacement of the dyes (14, 15). This study hinted that SWCNT fluorescence modulation might be controllable within a certain fluorescence resonance energy transfer distance from the SWCNT surface and potentially exploited for nanosensor development. However, a critical drawback of these dyes was their limited aqueous phase solubility—a typical characteristic of organic dyes—which often results in incompatibility with nanosensors that operate in aqueous environments. Recently, Zheng et al. observed a similar quenching effect from methylene blue (MB), a water-soluble fluorescent redox dye widely used as an electrochemical and fluorescent probe (16). Furthermore, as elaborated below, we found that, unlike ssDNA, this MB-induced fluorescence quenching remains stable in the presence of typical reducing molecules abundant in biological fluids. Thus, we hypothesized that MB could serve as a fluorescence resonance energy transfer-based modulator of SWCNT fluorescence that could be used to develop SWCNT-based nanosensors that exhibit high turn-on/off ratios and high selectivity to the target biomolecules.

Results and Discussion

To validate MB for developing quenching-based nanosensors, we investigated the properties of MB-mediated SWCNT fluorescence quenching. Fig. 1*A* illustrates representative NIR fluorescence spectra of $(GT)_{15}$-wrapped SWCNT with successive additions of 0, 30 nM, 100 nM, and 1 μM MB. As expected, MB instantaneously quenches SWCNT fluorescence in a dose-dependent manner. The normalized fluorescence changes ($\Delta F/F_0$) fit an isothermal adsorption curve, confirming that MB adsorption causes fluorescence quenching (Fig. 1*B*). Assuming full reversibility, SWCNT $\Delta F/F_0$ can potentially reach up to 3,000%, a value comparable to the best responses generated by SWCNT-based dopamine nanosensors (7). UV-vis-NIR absorption spectroscopy of SWCNT with 1 μM MB revealed no change in the SWCNT absorption profile, indicating a fluorescence quenching mechanism based on a photoinduced excited-state charge transfer (*SI Appendix*, Fig. S1) (15). Furthermore, the reported reduction potential of MB ranges from 0.01 to −0.88 V vs. SHE (standard hydrogen electrode), aligning well with the energy level favorable for this mechanism (17, 18). This feature is crucial for adsorption/desorption-induced reversibility, as ground-state charge transfer in contrast would result in fluorescence bleaching that is irreversible without the addition of reducing agents (14). To test this hypothesis, we tested and found that, removal of unbound MB from the solution resulted in partial reversal of fluorescence quenching, confirming that desorption of MB from the SWCNT surface can reverse the quenching effect (Fig. 1*C*).

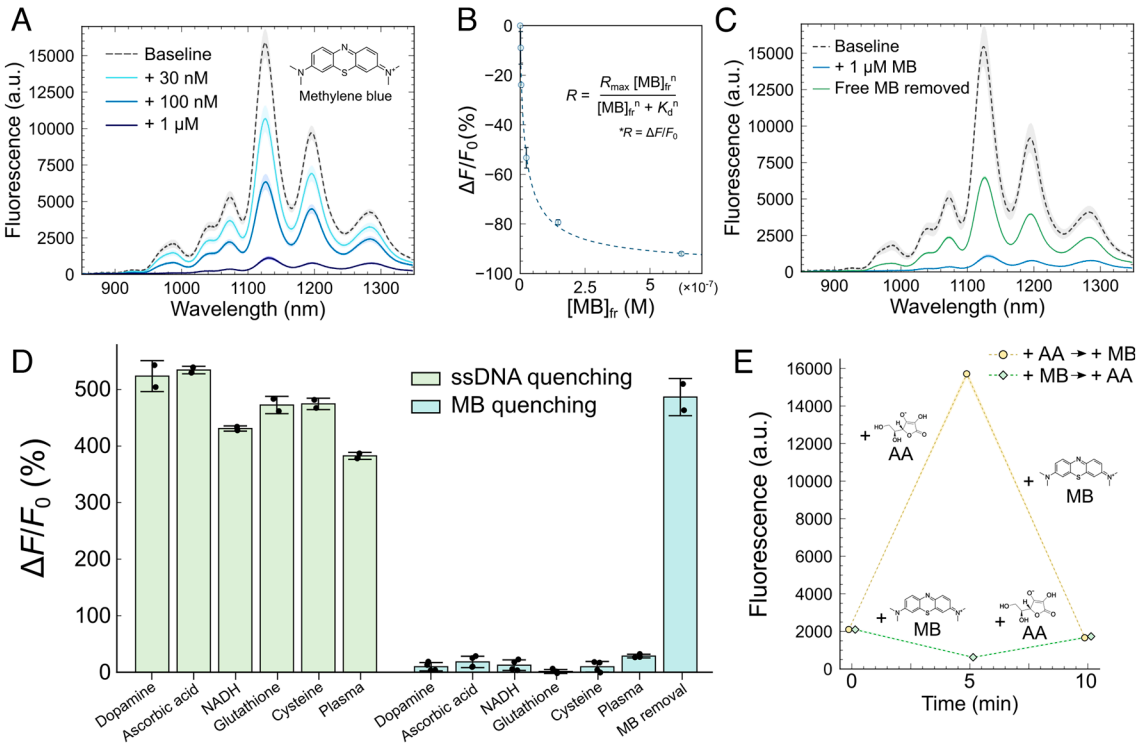

Fig. 1. Characterization of MB-induced fluorescence quenching of $(GT)_{15}$-SWCNTs. (*A*) Representative NIR fluorescence spectra of $(GT)_{15}$-SWCNT recorded 30 min after successive additions of 0, 30 nM, 100 nM, and 1 μM MB ($N = 3$). (*B*) Corresponding $\Delta F/F_0$ at (9,4) chirality peak plotted as a function of the unbound MB concentration at equilibrium, $[MB]_{fr}$ ($N = 2$, error bars represent SD). The determination of $[MB]_{fr}$ is detailed in *SI Appendix*, Supporting Text S1. (*C*) Average NIR fluorescence spectra ($N = 2$) of $(GT)_{15}$-SWCNT (gray), with 1 μM MB (30 min, blue), and 1 h after three rounds of spin filtration (green). Colored regions represent SD. (*D*) Average $\Delta F/F_0$ of $(GT)_{15}$-SWCNT (synthesized in 10 mM NaCl, green), and $(GT)_{15}$-SWCNT preincubated 1 h in 1 μM MB (synthesized in 1X PBS, blue) at (9,4) chirality peak, measured 5 min after the addition of 10 μM of various reducing molecules: dopamine, L-ascorbic acid, NADH, glutathione, and L-cysteine; and 0.1X human plasma ($N = 2$, error bars represent SD). (*E*) Fluorescence intensity changes upon addition of 1 μM MB and 10 μM ascorbic acid (AA) in different sequential orders ($N = 3$). All *N* represent individual batches of SWCNT conjugates.

Since fluorescence quenching is essentially an "oxidation" of SWCNT, reducing molecules are generally known to reverse the quenching effect of ssDNA (13). We therefore tested whether the addition of reducing molecules can recover fluorescence of MB-quenched SWCNT. Specifically, we examined the effect of several reducing molecules abundant in biological fluids (dopamine, L-ascorbic acid, NADH, glutathione, and L-cysteine) on MB-quenched SWCNT fluorescence, and compared MB-based quenching to ssDNA-based quenching. We also tested the effect of human plasma as an example of a complex biological fluid containing various redox molecules. For these assays, we mixed $(GT)_{15}$-SWCNT with 1 μM MB, the minimum MB concentration required to reach quenching saturation, and added 10-fold excess of reducing molecules. We also prepared a sample of $(GT)_{15}$-SWCNT alone, without MB, as described previously (9) and in *SI Appendix*, Fig. S2. As expected, all reducing molecules, including plasma, reversed ssDNA-based quenching, with $(GT)_{15}$-SWCNT $\Delta F/F_0$ ranging from 400 to 500% upon addition of these reducing molecules (Fig. 1*D* green and *SI Appendix*, Fig. S3). In contrast, these reducing molecules had minimal impact on the MB-quenched $(GT)_{15}$-SWCNT, with a maximum $\Delta F/F_0$ of 30% with the addition of plasma; thus, highlighting an important difference of MB from ssDNA in terms of redox-based reversibility (Fig. 1*D*, blue and *SI Appendix*, Fig. S3). Furthermore, we tested two representative oxidizing reagents, hydrogen peroxide (H_2O_2) and flavine adenine dinucleotide (FAD), and found negligible impact on the MB-quenched baseline (*SI Appendix*, Fig. S4). Importantly, the order of addition of the reducing molecule and MB did not affect the final fluorescence intensity of SWCNT, indicating that ssDNA- and MB-mediated quenching are independent of each other (Fig. 1*E*). Our results thus motivate the use of MB as a fluorescence mediator to develop NIR fluorescent nanosensors with rationally designed target-specificity.

The properties of MB-mediated fluorescence quenching, namely its insensitivity to redox environments and reversibility through desorption (Fig. 1*D*), led us to hypothesize that nanosensors with high selectivity could be rationally designed by coupling specific molecular recognition on SWCNTs to MB movement. To explore this strategy's viability, we engineered an SWCNT corona wherein DNA hybridization selectively modulates SWCNT fluorescence intensity through concurrent MB displacement. Our model system consisted of $(GT)_{15}T_{20}$-wrapped SWCNTs designed to hybridize with the target sequence, A_{20} (Fig. 2*A*) (19). We covalently conjugated MB to the hybridizing region (T_{20}), anticipating that A_{20} target binding would induce partial desorption of the double helix within the T_{20} domain, thereby displacing MB from the SWCNT surface (20, 21). To maximize surface displacement, MB was conjugated to the 3′-end of T_{20}. All ssDNA-wrapped SWCNTs were prepared using standard sonication-based dispersion in 1X PBS, conditions under which ssDNA does not quench SWCNT fluorescence, thus minimizing contributions from nonspecific turn-on responses (*SI Appendix*, Fig. S2).

To investigate whether A_{20} target binding induces desorption of the MB-tagged T_{20} target ssDNA hybridized on SWCNT, we first sought to quantify MB density on the SWCNT surface. MB itself is a fluorophore with excitation/emission wavelength peaks at 660/670 nm (22), and SWCNTs are known to be effective quenchers of fluorescent dyes (23–26). We therefore hypothesized that MB adsorption to SWCNTs could be quantified by measuring MB fluorescence without interference from SWCNT NIR fluorescence. We tested this hypothesis by comparing MB fluorescence

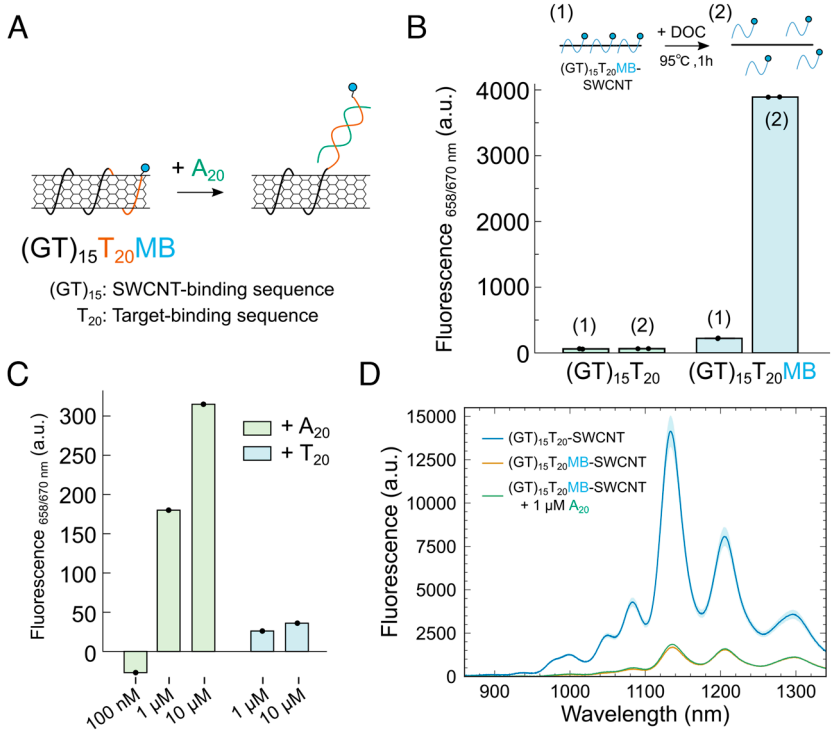

Fig. 2. Quantification of MB dynamics on SWCNTs. (*A*) Conceptual illustration of nanosensors comprising binder sequence: $(GT)_{15}$ and target-binding sequence: T_{20}. NIR fluorescence quencher dye MB is conjugated to the 3′-end of ssDNA. Hybridization of the complement sequence, A_{20}, induces partial desorption of the double-helix from the SWCNT surface, thereby modulating the NIR fluorescence intensity. (*B*) MB fluorescence (baseline subtracted) of ssDNA [*Left*: $(GT)_{15}T_{20}$ and *Right*: $(GT)_{15}T_{20}$MB] before 1) and after 2) desorption from SWCNT via surfactant-based surface exchange. $N = 2$ (technical replicates), with error bars representing SD. DOC: sodium deoxycholate. (*C*) Baseline subtracted MB fluorescence of $(GT)_{15}T_{20}$MB-SWCNT following dose-dependent addition of A_{20} (green) and T_{20} (blue). Measurements were performed 12 h after the addition of the analytes. (*D*) Average NIR fluorescence spectra of $(GT)_{15}T_{20}$-SWCNT (blue), $(GT)_{15}T_{20}$MB-SWCNT (orange), and $(GT)_{15}T_{20}$MB-SWCNT + 1 μM A_{20} (green, 12 h incubation). Spectra are averages of two individual batches, and the colored regions represent SD.

of $(GT)_{15}T_{20}$MB-SWCNT before and after complete ssDNA displacement from the SWCNT surface by surfactant-induced surface exchange. As expected, MB fluorescence increased from 220 a.u. when adsorbed in $(GT)_{15}T_{20}$MB-SWCNT format to 3,890 a.u. after surfactant-induced displacement of $(GT)_{15}T_{20}$MB from the SWCNT, representing 95% dequenching upon desorption from SWCNT and confirming the ability of SWCNTs to effectively quench MB fluorescence (Fig. 2*B*). Notably, 95% of adsorbed MB molecules were quenched, indicating that most of the $(GT)_{15}T_{20}$ ssDNA is adsorbed close to the SWCNT surface. Based on this assay, we estimated the number of MB molecules on SWCNTs to be 0.35 μmol per mg of SWCNTs (*SI Appendix*, Fig. S5). Next, we added target (A_{20}) and control (T_{20}) ssDNA sequences in a concentration-dependent manner to assess whether hybridization selectively displaces MB from the SWCNT surface. As expected, MB fluorescence increased selectively with the addition of 1 μM A_{20}, confirming target binding indeed drives desorption of hybridized complexes along with MB (Fig. 2*C*). However, this displacement of MB was not reflected in the SWCNT NIR fluorescence intensity, as the addition of 1 μM A_{20} resulted in only a slight $\Delta F/F_0$ = 15% intensity change (Fig. 2*D*). Nevertheless, equimolar addition of T_{20} generated $\Delta F/F_0$ = -7.5%, indicating that the NIR fluorescence intensity change upon A_{20} addition is a result of target binding.

DNA hybridization-induced MB displacement from the SWCNT surface was evidenced by MB dequenching fluorescence studies; however, this phenomenon failed to manifest in SWCNT NIR fluorescence intensity modulations. We hypothesized that the high density of MB molecules on SWCNTs resulted in insufficient total displacement to elicit detectable SWCNT fluorescence changes. In fact, comparing MB fluorescence of $(GT)_{15}T_{20}$MB-SWCNT + A_{20} with fully desorbed $(GT)_{15}T_{20}$MB revealed that even at maximum A_{20} concentration of 10 μM, only 6% of total MB molecules were displaced from SWCNT surfaces (Fig. 2 *B* and *C*). Thus, to amplify the transduction of MB displacement to SWCNT NIR fluorescence intensity changes, we implemented a strategy to regulate the MB molecule density on SWCNTs during sensor preparation, thereby enabling larger intensity changes from restricted quantities of MB being displaced (*SI Appendix*, Fig. S6). Specifically, we doped ssDNA-SWCNTs with unlabeled $(GT)_{15}$ as a spacer sequence during synthesis to modulate MB density on SWCNTs. In other words, ssDNA-SWCNT conjugates were synthesized with variable $(GT)_{15}$:$(GT)_{15}T_{20}$MB (m/m) ratios, presuming equivalent SWCNT binding affinities for both sequences.

As expected, a linear correlation was observed between percent $(GT)_{15}T_{20}$MB in the starting mixture and the number of $(GT)_{15}T_{20}$MB molecules on SWCNTs (*SI Appendix*, Fig. S5), thereby enabling precise control over MB density on SWCNTs and, consequently, baseline NIR fluorescence intensity of the constructs (Fig. 3*A*). Accordingly, maximal SWCNT fluorescence intensity transitions were identified in the 15 to 20% $(GT)_{15}T_{20}$MB range, suggesting that a 15 to 20% MB surface coverage—corresponding to 0.05-0.06 μmol per mg of SWCNTs—would induce maximal SWCNT response potential upon target binding (Fig. 3*B*). Notably, ssDNA-MB conjugates adsorbed to SWCNTs exhibited enhanced quenching efficiency compared to MB alone binding to SWCNTs, requiring fewer molecules in the former to achieve equivalent quenching levels (*SI Appendix*, Fig. S7).

Fig. 3*B* illustrates the $\Delta F/F_0$ responses (bottom axis, bar graph) and baseline fluorescence intensity (top axis, yellow points) of the (9,4) SWCNT chirality peak as a function of percent $(GT)_{15}T_{20}$MB, with representative spectra at 10, 15, and 40% shown on the right. As predicted from baseline fluorescence transition, $\Delta F/F_0$ peaked at 80% with 15% MB content upon addition of only 100 nM A_{20}. Complementary MB fluorescence assays confirmed that the number of displaced MB molecules is independent of percent $(GT)_{15}T_{20}$MB content, highlighting the importance of controlling MB prequenching molecule density in maximizing SWCNT $\Delta F/F_0$ responses (*SI Appendix*, Fig. S8). MB-free ssDNA-SWCNT constructs served as additional negative control, validating A_{20} response specificity to MB displacement from SWCNTs (*SI Appendix*, Fig. S9).

We subsequently investigated the position dependence of MB molecules within $(GT)_{15}T_{20}$ by modulating the MB conjugation site, denoted as $(GT)_{15}T_{20}$: (*n*), where MB is conjugated adjacent to the *n*th nucleotide (nt) base of $(GT)_{15}T_{20}$. Fig. 3*C* depicts $\Delta F/F_0$ of the SWCNT (9,4) chirality peak as a function of *n* (*n* = 1, 26, 28, 30, 50) (corresponding spectra shown in *SI Appendix*, Fig. S10). As expected, $\Delta F/F_0$ diminished as MB was repositioned from 3′ to 5′ ends of $(GT)_{15}T_{20}$, becoming negligible at *n* = 26 (i.e., 4 nucleotides 5′ from the start of the T_{20}). This result further implies that hybridization specifically displaces the hybridized region, while the "anchoring" portion of the ssDNA itself remains attached to SWCNTs (Fig. 2*A*), suggesting potential nanosensor reversibility. Notably, *n* = 28 and 30, positions near the $(GT)_{15}$-T_{20} interface that are predicted to allow minimal MB displacement, still exhibited considerable responses of 40% and 50% $\Delta F/F_0$, respectively. This suggests SWCNT fluorescence is highly sensitive to the distance of MB from the surface, and the

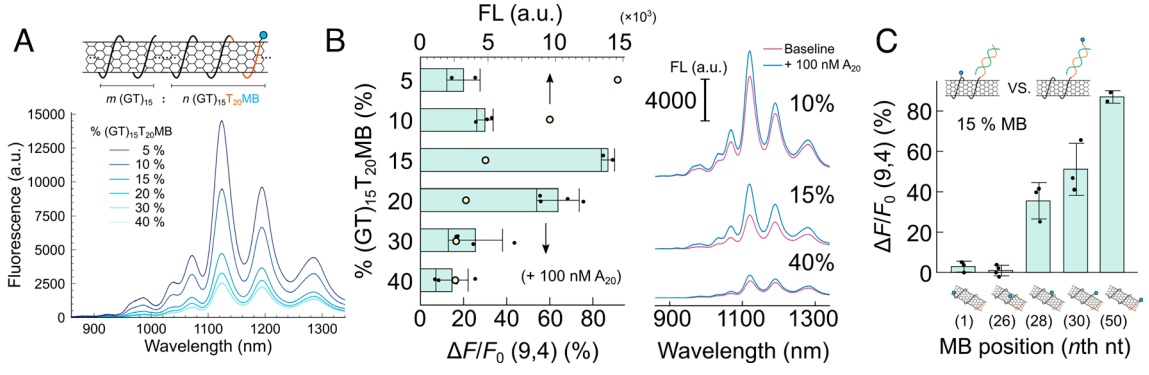

Fig. 3. Transduction of DNA hybridization on SWCNTs to NIR fluorescence modulations. (*A*) NIR fluorescence spectra of ssDNA-SWCNTs synthesized with variable $(GT)_{15}$:$(GT)_{15}T_{20}$MB ratios (5, 10, 15, 20, 30, and 40%). The top schematic illustrates the strategy to modulate MB density on SWCNTs by incorporating $(GT)_{15}$ as a spacer. (*B*) (*Left*, bar graph) Average $\Delta F/F_0$ responses of corresponding SWCNT constructs at (9,4) chirality peak after 12 h incubation with 100 nM A_{20}, as a function of percent $(GT)_{15}T_{20}$MB (left axis). Yellow dots represent baseline fluorescence intensity at (9,4) chirality peak (top axis). (*Right*) Representative fluorescence spectra of percent $(GT)_{15}T_{20}$MB = 10, 15, and 40% with (blue) and without (purple) 100 nM A_{20}. (*C*) $\Delta F/F_0$ responses of 15% $(GT)_{15}T_{20}$MB: (*n*)-SWCNTs at (9,4) chirality peak as a function of *n* (*n* = 1, 26, 28, 30, and 50). For *B* and *C*, *N* = 4, with data points represented by black dots; error bars represent SD. Each N represents an individual batch of SWCNT constructs.

flexibility of ssDNA near the hybridized region. Based on these studies, we find that SWCNT fluorescence modulation can occur within a physical distance of 6.8 nm from the SWCNT surface, assuming that the T_{20} domain, when fully hybridized to A_{20}, acts as an inflexible polymer (27). Collectively, these findings corroborate the feasibility of modulating SWCNT fluorescence intensity via MB movement linked to molecular recognition at the SWCNT surface.

These promising results motivated us to apply this technology to develop a versatile platform for oligonucleotide-detecting nanosensors. DNA and RNA oligonucleotides serve as substrates that indicate the presence of pathogens (28) and various diseases, including cancer (29) and neurodegenerative disorders (30). Consequently, NIR fluorescent oligonucleotide probes hold significant potential for diverse biomedical applications. Previously reported SWCNT-based NIR fluorescent nanosensors for oligonucleotides have been limited to signal transduction via unpredictable wavelength shifts of 1 and 2 nm (31) or surfactant-amplified wavelength (~10 nm) and/or intensity changes (32, 33)—methods that are challenging to translate to complex biological environments. Moreover, those approaches necessitate trial-and-error-based selection of appropriate target-binding sequences (33), compromising flexibility in rational nanosensor design. In this regard, our proposed design is capable of directly transducing DNA hybridization events on SWCNTs to fluorescence intensity changes, thus potentially enabling the development of a robust and versatile oligonucleotide detection platform. Notably, our nanosensor design decouples SWCNT dispersal from analyte detection. Our nanosensor incorporates a spacer sequence, conferring target-binding sequence-independent colloidal stability to the nanosensor constructs—a challenge typically encountered in conventional nanosensor designs. Furthermore, the target-binding sequence can be rationally designed to detect analytes of interest with high selectivity while minimally affecting sensor stability or fluorescence intensity changes.

Therefore, we sought to test the robustness and versatility of our MB dequenching-based platform by developing nanosensors with four distinct target-binding sequences to detect tobacco mosaic virus (TMV) in plants. TMV, a highly infectious plant virus, primarily affects tobacco, tomatoes, and other economically important crops, causing substantial yield losses in industry (34, 35). We selected four target RNA sequences of varying lengths (25 to 41 nt) from the TMV genome encoding coating protein. Our pilot study revealed that MB conjugation to the 3′-end of the TMV1 target-binding sequence [$(GT)_{15}$TMV1-MB_{55}] generated insufficient response to the target ssDNA, with only 10 to 20% $\Delta F/F_0$, despite well-quenched baseline fluorescence (*SI Appendix*, Fig. S11). The less effective quenching of $(GT)_{15}$TMV1-MB_{55} at comparable MB density on SWCNTs compared to $(GT)_{15}T_{20}$-MB indicated ineffective target-binding sequence binding on SWCNT, especially at the 3′ terminus, leading to only partial displacement of MB (36). Consequently, leveraging our finding that internally positioned MB within the target-binding sequence can induce effective SWCNT fluorescence modulation (Fig. 3*C*), we identified an optimal MB position 6 nucleotides 3′ from the start of the TMV target-binding sequence (i.e., 36th nucleotide within the whole sequence, as illustrated in Fig. 4 *A*, *Top*).

The NIR fluorescence spectra of 15% $(GT)_{15}$TMV1-MB_{36}-SWCNT [mixture of 15% $(GT)_{15}$TMV1-MB_{36} with 85% $(GT)_{15}$], revealed a robust response to the target ssDNA complement compared with control PBS, with $\Delta F/F_0$ at (9,4) chirality peaking at 60% for 1 μM ssDNA (Fig. 4*A*). This sensitivity and selectivity was further validated across all nanosensor variants, each responding specifically to its target ssDNA while remaining inert to scrambled controls (*SI Appendix*, Fig. S12). Notably, even TMV4, despite its extended nucleotide length (41 nt target-binding sequence, 71 nt total), maintained selectivity with a $\Delta F/F_0$ of 30%. Investigation of chirality dependence revealed that SWCNTs with shorter diameters generally produced larger $\Delta F/F_0$, exceeding 100% for (6,5) chirality species in TMV1 and TMV2 (Fig. 4*B* and *SI Appendix*, Fig. S13; see *SI Appendix*, Fig. S14 for peak deconvolution). Next, we assessed the nanosensors' efficacy in recognizing extended DNA and RNA oligonucleotides. The $\Delta F/F_0$ responses of (7,5) chirality nanosensors were evaluated against a panel of analytes, including 90 nt target ssDNA with multiple binding domains (TMV1 and TMV3), and 30 nt ssRNA (complement and scrambled) for TMV1 (Fig. 4*C*). The results demonstrate appreciable sensitivity and selectivity of the nanosensors to long ssDNA fragments and ssRNAs, whereby the same TMV oligonucleotides but in a scrambled sequence do not modulate SWCNT fluorescence intensity. Notably,

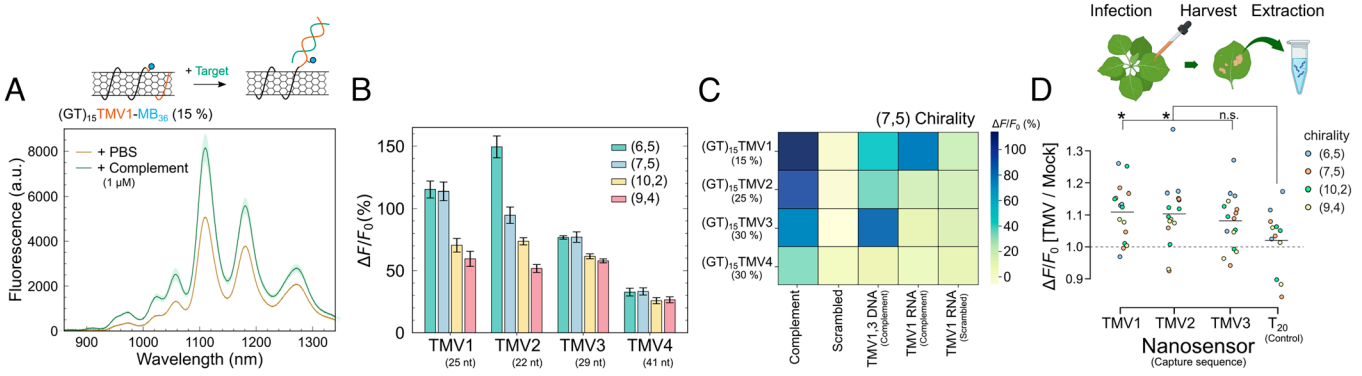

Fig. 4. Development of an SWCNT-based versatile platform for oligonucleotide detection. (*A*) NIR fluorescence spectra of $(GT)_{15}$TMV1-SWCNT following addition of 1X PBS (orange) and 1 μM target ssDNA (green) (N = 2, with colored regions representing SD). (*B*) Chirality-dependent integrated $\Delta F/F_0$ responses following incubation with 1 μM target ssDNA as a function of different nanosensors (N = 2, with error bars indicating SD). (*C*) Heat map representing integrated $\Delta F/F_0$ at (7,5) chirality spectrum as a function of different nanosensors and 1 μM of varying analytes: complement target ssDNA, scrambled ssDNA, 90 nt long target ssDNA including binding domains for TMV1 and TMV3, 30 nt target ssRNA including TMV1-binding domain, and its scrambled sequence (N = 2). All data in (*A*–*C*) were collected after 24 h of incubation postanalyte addition. Each N represents a distinct nanosensor batch. (*D*) Detection of endogenous TMV-originating oligonucleotides in *Nicotiana benthamiana* leaf extracts. The figure represents the integrated $\Delta F/F_0$ ratios after treatment with the DNA/RNA samples extracted from TMV-infected and mock control plant leaves as a function of nanosensors with target-binding sequences: TMV1, TMV2, TMV3, and T_{20}. The concentration of the sample was normalized to 0.1 mg/mL using oligonucleotide absorbance at 260 nm. Data were acquired after 48 h of incubation. Each plot represents an average of three to five technical replicates, with a total of four biological replicates. Each color represents a specific chirality. Horizontal lines indicate the mean value of the entire dataset. Statistical comparisons between each TMV nanosensor and the control were conducted using Welch's t test with a significance threshold of $P < 0.05$.

$(GT)_{15}$TMV1-SWCNT detected 90 nt ssDNA in a dose-dependent manner down to 10 nM (*SI Appendix*, Fig. S15). Corresponding fluorescence spectra and comprehensive chirality comparisons are presented in *SI Appendix*, Figs. S16 and S17.

Subsequently, we demonstrate the potential applicability of our nanosensors as a diagnostic tool for TMV infection in crops. We employed *N. benthamiana* as a plant model, subjecting it to TMV infection alongside mock controls. Following a 1- to 2-wk incubation period (*SI Appendix*, Fig. S18), we harvested infected leaves and extracted nucleic acids by CTAB purification. The diluted extracts were mixed with nanosensors without further purification or amplification, followed by NIR fluorescence characterization. The efficacy of our approach is evidenced in Fig. 4*D*, which presents the $\Delta F/F_0$ ratios of TMV-infected versus mock samples across three TMV-specific nanosensors and one control mock nanosensor lacking the TMV target-binding sequence. The consistent observation of $\Delta F/F_0$ SWCNT fluorescence ratios exceeding 1 for TMV nanosensors, contrasted with significantly smaller values for the mock nanosensor control, provides compelling evidence of successful endogenous TMV-derived oligonucleotide detection. Meanwhile, significant variation in the $\Delta F/F_0$ ratios was observed, likely due to fluctuations in viral RNA concentrations and inherent biological variability of working with biofluid samples, which is reflected in the variable nanosensor sensitivity. Using RT-qPCR, we estimated the viral RNA concentration in the samples to be between 0.1 and 0.5 ng/μL, indicating the need for further refinement of the nanosensor design to achieve very early viral detection.

Finally, we sought to demonstrate the broader applicability of MB-mediated fluorescence quenching for designing nanosensors targeting analytes beyond oligonucleotides. We hypothesized that a target molecule binding to a receptor conjugated to $(GT)_{15}$ could trigger MB displacement. To test this concept, we employed the biotin-avidin system as a model receptor–target pair, conjugating biotin to the 3′-end of $(GT)_{15}A_6$. In this design, A_6 serves as a linker, with MB conjugated to the 32nd nucleotide of the sequence.

Fig. 5*A* illustrates the NIR fluorescence spectra of 20% $(GT)_{15}A_6MB_{32}$-Biotin-SWCNT upon incubation with biotin-binding neutravidin, or control protein bovine serum albumin (BSA). As anticipated, the addition of 100 nM neutravidin induced a remarkable 100% increase in the SWCNT fluorescence intensity, contrasting with the modest 10% SWCNT fluorescence increase observed with the BSA control. While slight variations in response magnitude were noted, all biotin-binding proteins (avidin and streptavidin) elicited responses from the nanosensor (*SI Appendix*, Fig. S19 and Fig. 5*B*, green). To validate the mechanism underlying this response, we synthesized nanosensors using the same sequence but lacking either the MB quencher or the biotin recognition element. These control nanosensors exhibited minimal responses to neutravidin and BSA, confirming that the observed fluorescence intensity increase is indeed driven by neutravidin-biotin binding-induced MB displacement (Fig. 5*B*). Importantly, our design maintains its insensitivity to redox molecules, which normally strongly and indiscriminately modulate SWCNT fluorescence. The insensitivity of our MB-based SWCNT nanosensors to redox molecules highlights the potential utility of our platform for developing highly selective nanosensors that overcome issues of SWCNT nanosensor indiscriminate fluorescence modulation upon exposure to biofluids (Fig. 5*C* and *SI Appendix*, Fig. S20). The results herein indicate the potential expansion of our platform by conjugating various recognition units—such as MB-tagged aptamers, antibodies, or nanobodies, to create highly selective SWCNT-based NIR fluorescent probes.

Conclusions

In this study, we developed a SWCNT-based nanosensor platform that harnesses the unique properties of dye-mediated fluorescence quenching. In particular, we leveraged the ability of methylene blue (MB) to effectively quench SWCNT fluorescence. We found that this quenching occurs through an adsorption-driven photoinduced charge transfer mechanism, which is reversible upon MB displacement from the SWCNT surface. We quantify the magnitude of this photoinduced charge transfer mechanism and calculate that SWCNTs are sensitive to MB proximity within a FRET distance of 6.8 nm of their surface. The remarkable stability of MB's quenching effect in redox environments sets it apart from quenching by other common dispersants such as ssDNA-based quenching, motivating its use as a fluorescence mediator for robust nanosensor designs and future in vivo use. As a proof-of-concept, we engineered an SWCNT corona with ssDNA comprising an SWCNT-binding sequence $(GT)_{15}$, followed by a target-binding sequence T_{20}, with MB conjugated to the 3′-end of T_{20}, under the hypothesis that target binding would induce the desorption of the hybridized complex along with

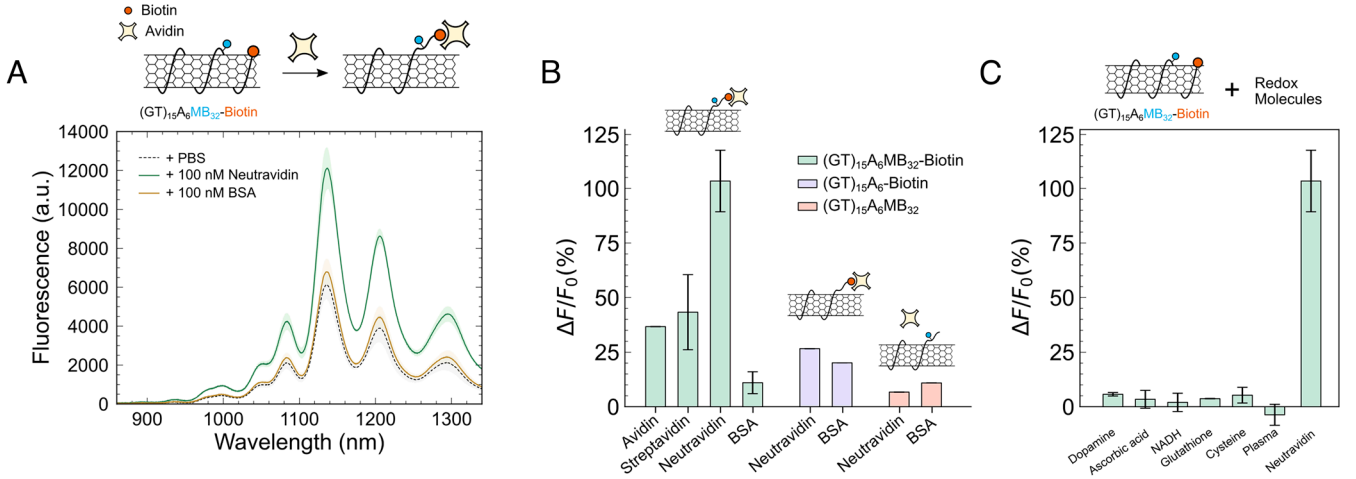

Fig. 5. Biomolecule recognition leveraging the dye-quenching mechanism. (*A*) NIR fluorescence spectra of 20% $(GT)_{15}A_6MB_{32}$-Biotin-SWCNT without analyte (black), with 100 nM neutravidin (green), and with 100 nM BSA (orange). Data were collected 12 h after addition of the target proteins or buffer alone. (*B*) $\Delta F/F_0$ responses of 20% $(GT)_{15}A_6MB_{32}$-Biotin-SWCNT (green), 20% $(GT)_{15}A_6$-Biotin-SWCNT (purple), and 20% $(GT)_{15}A_6MB_{32}$SWCNT (pink) ($N = 2$, error bars represent SD). (*C*) $\Delta F/F_0$ responses of 20% $(GT)_{15}A_6MB_{32}$-Biotin-SWCNT following the addition of 10 μM reducing molecules: dopamine, ascorbic acid, glutathione, cysteine, and 0.1X plasma as final concentrations ($N = 2$, error bars represent SD). All *N* represent individual nanosensor batches.

the conjugated MB. After confirming hybridization-induced MB displacement via MB fluorescence, we precisely controlled MB density on SWCNTs by incorporating $(GT)_{15}$ as a spacer, achieving a maximum $\Delta F/F_0$ response of 80% to the target sequence alone. Expanding on these initial findings, we developed a robust and versatile platform for oligonucleotide detection, using TMV as a model pathogen. By optimizing MB position within the target-binding sequence, we demonstrated the sequence- and length-independent development of four distinct TMV probes capable of selectively detecting their complement target sequences with $\Delta F/F_0$ exceeding 100% at specific SWCNT chiralities. We successfully applied these nanosensors to distinguish TMV-infected plants from mock controls. Finally, we demonstrated the potential expansion of our design to target a wider scope of molecular recognition elements using the biotin-avidin system as a model. By attaching biotin to the MB-conjugated ssDNA, we developed a sensor that could selectively and robustly respond to biotin-binding proteins through the same MB displacement mechanism as our oligonucleotide nanosensors, without promiscuous fluorescence modulation by redox-active molecules. In future studies, optimizing the design of the SWCNT corona could mitigate slow response kinetics, thereby broadening the potential applications of this technology. Furthermore, integrating anti-biofouling properties into the nanosensor design would enhance the feasibility for nanosensor applications in complex biological environments. Our study therefore presents a generalizable platform that enables rational engineering of SWCNT NIR fluorescence intensity, potentially overcoming intrinsic selectivity challenges of existing SWCNT nanosensors for more seamless applications across diverse biological systems.

Materials and Methods

Synthesis of Methylene Blue–Conjugated ssDNA Oligonucleotides. Lyophilized, primary amine-modified ssDNA oligonucleotides were purchased from IDT, with a full list of sequences provided in Supporting Information (*SI Appendix*, Fig. S21). 30 OD ssDNA was dissolved in 0.2 mL of a pH 8.5, 0.091 M sodium tetraborate (Sigma-Aldrich S9640) buffer. Then, 50 μL of 14 mM methylene blue-NHS ester (Sigma-Aldrich 43499) in DMSO was mixed with ssDNA in a 2 mL DNA low-bind tube. The mixture was placed on a rotary shaker at 20 rpm for 2 h. For purification, 1 mL of ethanol/3M sodium acetate (Sigma-Aldrich S2889) (9:1 V/V) was added to the mixture, and centrifuged for 20 min at 13,000 rpm at 12 °C using a microcentrifuge (Eppendorf 5425 R). The precipitate was washed two times by gently swirling in ice-cold 70% ethanol. The final pellet was vacuum-dried and stored at −20 °C as a 5 mg/mL aliquot in water. Typical synthesis yielded 90% ssDNA conjugate with conjugation efficiency varying from 80 to 90% (quantified by MB fluorescence at ex/em = 658/670 nm and oligonucleotide absorbance at 260 nm using Nanodrop).

Synthesis of ssDNA-Wrapped SWCNT Dispersion. Single-stranded DNA oligonucleotides (5 mg/mL aliquot in water) were mixed with HiPCO SWCNT (Nanointegris; 2 mg/mL stock in water) in 1X PBS or 10 mM NaCl to a final volume of 1.2 mL and concentrations of 0.2 mg/mL and 0.1 mg/mL, respectively. 10 mM NaCl was used only for the ssDNA-quenched $(GT)_{15}$-SWCNT samples. The mixture was sonicated in an ice bath using an ultrasonicator (CPX 130, Sonics & Materials) for 30 min at 6 W. Then, the sample was centrifuged for 4 h at a rate of 21,000×*g* and under 4 °C. 1 mL of the top supernatant was collected, and the centrifugation was repeated at a 30-min cycle until the minimal pellets were observed. Centrifuged samples were stored under 4 °C without further purification for long-term storage for up to 3 mo. Unbound ssDNA was removed by performing four rounds of spin filtration using a 100 kDa spin column (Amicon Ultra) in until no detectable ssDNA remained in the flowthrough. The final concentration of SWCNT was determined by absorbance at 632 nm and stocked as 50 mg/L aliquot. Purified nanosensors were used within 2 wk. For the nanosensor synthesis, $(GT)_{15}$ (5 mg/mL aliquot in water) was mixed with MB-conjugated ssDNA with an appropriate ratio to a total concentration of 0.2 mg/mL.

Near-Infrared Fluorescence Spectroscopy. NIR fluorescence spectroscopy was performed using a custom-built, inverted Zeiss microscope (Axio Observer.D1, 10X objective) with a 721 nm excitation laser source coupled to a short-wavelength IR spectrometer (Princeton Instruments, SCT 320) and InGaAs detector (PyLoN-IR). SWCNT NIR emission was collected within 850 to 1,350 nm wavelength at 500 ms exposure time. In a typical experiment, SWCNT nanosensor stock was diluted to 1 mg/L in 1X PBS, and 99 μL was placed in a 384-well plate. Then, 1 μL of 100X concentrated analyte solution was added during the measurement. Conditions specific to the measurement are mentioned in the corresponding figure captions. All redox molecules (dopamine hydrochloride, sodium L-ascorbate, NADH, glutamate, and L-cysteine) and biotin-binding proteins (avidin, streptavidin, and neutravidin) were purchased from Sigma-Aldrich. Recovered plasma from pooled human donors was purchased from Medix Biochemica USA Inc. and centrifuged for 20 min at 4 °C before the measurements. For ssDNA (T_{20}) and biotin-binding protein measurements, fluorescence readings were taken after 12 h incubation to account for the ssDNA desorption kinetics (21). For longer TMV sequences where hybridization kinetics are slower, measurements were taken after 48 h incubation.

ssDNA Desorption and MB Fluorescence Assay. A ssDNA-SWCNT stock was diluted to a 50 μL of 10 mg/L in 1% sodium deoxycholate (DOC; Sigma-Aldrich D6750), 1X PBS. The mixture was heated at 95 °C for 1 h using the T100™ thermal cycler (BIO-RAD). Then, 50 μL 1X PBS was added to adjust the volume of the sample to 100 μL, followed by the fluorescence measurement (ex/em = 658/670 nm) in a 96-well plate using a plate reader (Infinite M Plex, Tecan. Each data point was generated as an average of 16 measurements, splitting each well into 4 × 4 regions. When MB fluorescence measurements were performed without desorption of ssDNA, SWCNT stock was diluted to 100 μL of 5 mg/L in 1X PBS with appropriate concentration of analytes.

Plant Growth and Maintenance. Plants were grown in a growth chamber set at a temperature of 24 °C, a light intensity of 100 to 150 μmol m^{-2} s^{-1}, and a photoperiod of 16 h light/8 h dark. *N. benthamiana* seeds were surfaced-sterilized using 15% bleach and 0.1% Tween-20, washed in H_2O, and suspended in 1% agar before planting. Seeds were sown in Sunshine Mix #4 soil (Sun Gro® Horticulture) and allowed to germinate in the growth chamber for 7 d. Healthy seedlings were transferred individually to 10 cm pots for further growth. Fertilization was done on a weekly basis with 75 ppm N 20–20–20 general-purpose fertilizer and 90 ppm N calcium nitrate fertilizer reconstituted in water.

Viral Infection. TMV strain U1 (TMV-U1) was used as the viral pathogen. The viral sap stock inoculum was prepared by macerating TMV-U1-infected *Nicotiana Tabacum* L. cv. Petite Havana SR1 leaf tissue, resuspending the tissue in 20 mM sodium phosphate buffer (pH 7.0), and storing the resulting stock in a freezer at −80 °C. Viral sap stocks had approximately >7 to 53 μg viral particles/mL (as determined by qRT-PCR).

Viral inoculations were performed based on a previously described method (37) and described briefly below. 4- to 5-wk-old *N. benthamiana* plants were used for the TMV infection experiments. 5 to 10 μL of viral sap stock was pipetted onto the mid-vein of the third and fourth oldest true leaves. The sap was gently rubbed from the mid-vein outward using a gloved hand. After several minutes, the remaining sap was rinsed off the leaves with milliQ water using a squirt bottle. A similar procedure was done for mock-infected plants, but milliQ water was used instead of viral sap. Infected and mock-infected plants were placed in an isolated growth room to grow over 10 to 14 d.

Tissue Collection and Processing. 10 to 14 d after infection, 2 to 3 systemic leaves that were not inoculated originally but exhibited viral symptoms, were collected per plant and frozen at −80 °C until processed. DNA was extracted using a standard CTAB (Cetyltrimethylammonium bromide) protocol briefly described hereafter. Tissue was ground using one of two methods: tissue was placed in plastic tubes using 3.2 mm chrome steel disruption beads (Research Products International Corp.) and the tissue was pulverized by running a Mini-Beadbeater-16 (BioSpec Products, Inc.) for 30 s; or tissue was ground using a mortar and pestle that had been cooled with liquid nitrogen. 500 μL of CTAB solution (2% CTAB, 100 mM Tris-HCl pH 8, 20 mM EDTA pH 8, 1.5 M NaCl, and 1% polyvinylpyrrolidone) were added per 100 mg of tissue and incubated at 65 °C for 10 min for extraction. An equal volume of chloroform:isopropanol (39:1) was added to the CTAB extract, mixed, and centrifuged for 10 min at 3,200×*g*. The aqueous phase was combined with 0.7 volumes of isopropanol to precipitate

the nucleic acids. After 10 min, the precipitated nucleic acids were collected by centrifugation at 3,200×*g* for 10 min. The pellet was washed once with 70% ethanol, and dried. Finally, the pellet was resuspended in PBS for analysis and stored at −80 °C. NIR fluorescence characterization was conducted under blinded conditions, ensuring that the virus and mock samples were indistinguishable during analysis. The total RNA concentration was normalized to 0.1 mg/mL, and 2 μL of the nanosensor stock (50 mg/L) was mixed with 98 μL of the purified sample, followed by incubation for 48 h before measurement.

Data, Materials, and Software Availability. All study data are included in the article and/or *SI Appendix*.

ACKNOWLEDGMENTS. We would like to thank Dr. Barbara Baker, Jeffrey Tung, and Shawna Kelley for the TMV-U1 strain and Nicotiana Tabacum cultivar Petite Havana SR1 seeds. We acknowledge support of a Chan Zuckerberg Initiative Imaging Award, a Burroughs Wellcome Fund Career Award at the Scientific Interface (to M.P.L.), the Philomathia Foundation (to M.P.L.), a Dreyfus Foundation award (to M.P.L.), the Philomathia Foundation (to M.P.L.), an NIH Maximizing Investigators' Research Award (to M.P.L.), an NIH Small Research Grants (R03) (to M.P.L.), an NSF Faculty Early Career Development Program (to M.P.L.), an NSF Division of Chemical, Bioengineering, Environmental and Transport Systems (to M.P.L.), an NSF Center for Genetically Encoded Materials award (to M.P.L.), a Sloan Foundation Award (to M.P.L.), a Moore Foundation Award (to M.P.L.), and a McKnight Scholar Award (to M.P.L.). M.P.L. is a Chan Zuckerberg Biohub investigator, a Hellen Wills Neuroscience Institute Investigator, and an IGI Investigator.

Author affiliations: [a]Department of Chemical and Biomolecular Engineering, University of California, Berkeley, CA 94720; [b]Hellen Wills Neuroscience Institute, University of California, Berkeley, CA 94720; [c]Innovative Genomics Institute, Berkeley, CA 94720; [d]California Institute for Quantitative Biosciences, QB3, University of California, Berkeley, CA 94720; and [e]Chan-Zuckerberg Biohub, San Francisco, CA 94158

1. M. J. O'Connell *et al.*, Band gap fluorescence from individual single-walled carbon nanotubes. *Science* **297**, 593–596 (2002).
2. F. Wang, G. Dukovic, L. E. Brus, T. F. Heinz, The optical resonances in carbon nanotubes arise from excitons. *Science* **308**, 838–841 (2005).
3. P. W. Barone, S. Baik, D. A. Heller, M. S. Strano, Near-infrared optical sensors based on single-walled carbon nanotubes. *Nat. Mater.* **4**, 86–92 (2005).
4. D. A. Heller *et al.*, Peptide secondary structure modulates single-walled carbon nanotube fluorescence as a chaperone sensor for nitroaromatics. *Proc. Natl. Acad. Sci. U.S.A.* **108**, 8544–8549 (2011).
5. S. Kruss *et al.*, Neurotransmitter detection using corona phase molecular recognition on fluorescent single-walled carbon nanotube sensors. *J. Am. Chem. Soc.* **136**, 713–724 (2014).
6. J. H. Choi, M. S. Strano, Solvatochromism in single-walled carbon nanotubes. *Appl. Phys. Lett.* **90**, 223114 (2007).
7. A. G. Beyene *et al.*, Ultralarge modulation of fluorescence by neuromodulators in carbon nanotubes functionalized with self-assembled oligonucleotide rings. *Nano Lett.* **18**, 6995–7003 (2018).
8. A. G. Beyene *et al.*, Imaging striatal dopamine release using a nongenetically encoded near infrared fluorescent catecholamine nanosensor. *Sci Adv* **5**, eaaw3108 (2019).
9. S. J. Yang, J. T. Del Bonis-O'Donnell, A. G. Beyene, M. P. Landry, Near-infrared catecholamine nanosensors for high spatiotemporal dopamine imaging. *Nat. Protoc.* **16**, 3026–3048 (2021).
10. C. Bulumulla *et al.*, Visualizing synaptic dopamine efflux with a 2D composite nanofilm. *eLife* **11**, e78773 (2022).
11. S. Jeong *et al.*, High-throughput evolution of near-infrared serotonin nanosensors. *Sci Adv* **5**, eaay3771 (2019).
12. C. P. Horoszko, P. V. Jena, D. Roxbury, S. V. Rotkin, D. A. Heller, Optical voltammetry of polymer-encapsulated single-walled carbon nanotubes. *J. Phys. Chem. C Nanomater. Interfaces* **123**, 24200–24208 (2019).
13. E. Polo, S. Kruss, Impact of redox-active molecules on the fluorescence of polymer-wrapped carbon nanotubes. *J. Phys. Chem. C* **120**, 3061–3070 (2016).
14. M. J. O'Connell, E. E. Eibergen, S. K. Doorn, Chiral selectivity in the charge-transfer bleaching of single-walled carbon-nanotube spectra. *Nat. Mater.* **4**, 412–418 (2005).
15. B. C. Satishkumar *et al.*, Reversible fluorescence quenching in carbon nanotubes for biomolecular sensing. *Nat. Nanotechnol.* **2**, 560–564 (2007).
16. Y. Zheng, A. A. Alizadehmojarad, S. M. Bachilo, A. B. Kolomeisky, R. B. Weisman, Dye quenching of carbon nanotube fluorescence reveals structure-selective coating coverage. *ACS Nano* **14**, 12148–12158 (2020).
17. Y. Y. Lee *et al.*, Visible-light driven photocatalytic degradation of organic dyes over ordered mesoporous $Cd_xZn_{1-x}S$ materials. *J. Phys. Chem. C, Nanomater. Interfaces* **121**, 5137–5144 (2017).
18. H.-E. Jacob, "Chapter IV: Redox potential" in *Methods in Microbiology* (Elsevier, 1970), pp. 91–123.
19. J. T. Metternich *et al.*, Near-infrared fluorescent biosensors based on covalent DNA anchors. *J. Am. Chem. Soc.* **145**, 14776–14783 (2023).
20. S. Jung *et al.*, Dissociation of single-strand DNA: Single-walled carbon nanotube hybrids by Watson–Crick base-pairing. *J. Am. Chem. Soc.* **132**, 10964–10966 (2010).
21. E. S. Jeng, P. W. Barone, J. D. Nelson, M. S. Strano, Hybridization kinetics and thermodynamics of DNA adsorbed to individually dispersed single-walled carbon nanotubes. *Small* **3**, 1602–1609 (2007).
22. A. Matsui *et al.*, Real-time, near-infrared, fluorescence-guided identification of the ureters using methylene blue. *Surgery* **148**, 78–86 (2010).
23. Z. Zhu *et al.*, Single-walled carbon nanotube as an effective quencher. *Anal. Bioanal. Chem.* **396**, 73–83 (2010).
24. R. Yang *et al.*, Carbon nanotube-quenched fluorescent oligonucleotides: Probes that fluoresce upon hybridization. *J. Am. Chem. Soc.* **130**, 8351–8358 (2008).
25. R. L. Pinals *et al.*, Quantitative protein corona composition and dynamics on carbon nanotubes in biological environments. *Angew. Chem. Int. Ed Engl.* **59**, 23668–23677 (2020), 10.1002/anie.202008175.
26. K. Umemura, S. Sato, G. Bustamante, J. Y. Ye, Using a fluorescence quenching method to detect DNA adsorption onto single-walled carbon nanotube surfaces. *Colloids Surf. B, Biointerfaces* **160**, 201–206 (2017).
27. C. Bustamante, Z. Bryant, S. B. Smith, Ten years of tension: Single-molecule DNA mechanics. *Nature* **421**, 423–427 (2003).
28. K. Kalimuthu *et al.*, Point of care diagnosis of plant virus: Current trends and prospects. *Mol. Cell. Probes* **61**, 101779 (2022).
29. P. S. Mitchell *et al.*, Circulating microRNAs as stable blood-based markers for cancer detection. *Proc. Natl. Acad. Sci. U.S.A.* **105**, 10513–10518 (2008).
30. S. Li, Z. Lei, T. Sun, The role of microRNAs in neurodegenerative diseases: A review. *Cell Biol. Toxicol.* **39**, 53–83 (2023).
31. J. Cui *et al.*, Understanding oligonucleotide hybridization and the role of anchoring on the single-walled carbon nanotube corona phase for viral sensing applications. *J. Phys. Chem. C* **127**, 606–620 (2023).
32. J. D. Harvey *et al.*, A carbon nanotube reporter of miRNA hybridization events in vivo. *Nat. Biomed. Eng.* **1**, 0041 (2017).
33. A. Hendler-Neumark, V. Wulf, G. Bisker, Single-walled carbon nanotube sensor selection for the detection of microRNA biomarkers for acute myocardial infarction as a case study. *ACS Sens.* **8**, 3713–3722 (2023).
34. K.-B.G. Scholthof, Tobacco mosaic virus: A model system for plant biology. *Annu. Rev. Phytopathol.* **42**, 13–34 (2004).
35. C. Hossain, V. Hernandez, L. McHugh, P.-T. Tran, B. Nash, Analyzing the impacts of tobacco mosaic virus on the microbial diversity of *Nicotiana benthamiana*. *J. Plant Pathol.* **104**, 959–967 (2022).
36. Y. Zheng, A. A. Alizadehmojarad, S. M. Bachilo, R. B. Weisman, Guanine-specific chemical reaction reveals ssDNA interactions on carbon nanotube surfaces. *J. Phys. Chem. Lett.* **13**, 2231–2236 (2022).
37. S. Whitham, S. McCormick, B. Baker, The N gene of tobacco confers resistance to tobacco mosaic virus in transgenic tomato. *Proc. Natl. Acad. Sci. U.S.A.* **93**, 8776–8781 (1996).